Progress In Electromagnetics Research B, Vol. 102, 81–98, 2023

Improved Non-Singular Fast Terminal Sensor-Less Sliding Mode Control of IPMSM Considering External Disturbance and Parameter Perturbation

Xiangfei Li, Junqin Liu, Kaihui Zhao, Yang Yin, and Lihua Zou*

Abstract—A new non-singular fast terminal sensor-less sliding mode control algorithm (INFTSMC) for IPMSM based on an improved extended sliding mode disturbance observer (IESMDO) is constructed to address the problem of degraded control performance of IPMSM because of uncertainties. Firstly, a mathematical model of IPMSM under parametric ingestion is developed, and a new control law for the speed loop is designed. Then, an improved non-singular fast terminal sliding mode speed controller (INFTSMC) based on a novel extended sliding mode disturbance observer (IESMDO) is designed, where an improved super-twisting control law is designed to speed up convergence, while IESMDO can accurately observe the unknown perturbed part F of the system in real-time relative to the sliding mode disturbance observer (SMO). Finally, high-order square root cubature Kalman-filter (CKF) combined with an adaptive estimator is proposed to accurately estimate the speed and rotor position of the motor in real-time. Through simulations and semi-physical experiments with PI and traditional NFTSMC, it is verified that the algorithm has better transient steady-state performance when external disturbances and parameter perturbation are added externally to the motor, which is conducive to improve the control effect of IPMSM.

1. INTRODUCTION

Interior permanent magnet synchronous motor (IPMSM) has gained wide attention in electric vehicles because of its excellent control performance [1]. Currently, proportional-integral (PI) control is widely used in industry due to the advantages of simple algorithms [2]. However, IPMSM is susceptible to uncertainties such as unknown perturbations because its system is nonlinear. The traditional PI control strategy has the disadvantage of integral saturation, which is not easy to meet the current industrial requirements for the high precision performance of IPMSM control systems [3]. In recent years, to meet the demand for high-performance IPMSM in engineering applications, various advanced control methods such as predictive control [4], sliding mode control [5], and neural network control [6] have been proposed in academia. Among them, sliding mode control (SMC) is simple and robust to external disturbances, but it is difficult to suppress jitter.

To speed up the convergence and enhance the robustness of the control system, [7] introduced dynamic integration into the sliding mode control to achieve the effect of weakening the jitter, but the speed tracking performance of the control system is poor when the external disturbance is too large. In [8], a non-singular terminal sliding mode control strategy is proposed based on the traditional terminal sliding mode control, which enables the singularity problem to be solved and improves the response speed of the system, but the tracking performance of the system is poor. In [9], a sliding mode control method based on fractional order sliding mode surface is proposed to design a new convergence

Received 2 May 2023, Accepted 1 August 2023, Scheduled 13 August 2023
* Corresponding author: Lihua Zou (zoulihua0518@163.com).
The authors are with the College of Electrical and Information Engineering, Hunan University of Technology, Zhuzhou 412007, China.

law using fractional order symbolic functions, which effectively suppresses the jitter phenomenon existing in the system, but the algorithm for setting fuzzy rules is complicated. A new adaptive sliding mode convergence law is proposed in [10], which effectively suppresses the jitter of the control output while being able to dynamically adapt to the changes of the controlled system. Conventional speed control systems contain sensors, resulting in poor system reliability under special operating conditions. With the advancement of technology, velocity-free sensors are attracting attention because of their low cost and high interference immunity [11]. In [12], a Modified unscented Kalman filter (UKF) was used to improve the spherical sampling rule, but the accuracy of the observation under sudden load changes was not verified. Ref. [13] improves an extended Kalman filter (EKF) observer by introducing an adaptive fading factor, which can still be estimated accurately under sudden load change conditions. Ref. [14] presents an improved cubature Kalman filter (CKF) for the estimation of speed and rotor position of linear motors. In [13, 14], they combine the square root algorithm and time-varying noise valuator, which significantly improves the accuracy, but none of them consider the complex operating conditions where the other parameters of the motor vary.

In response to the above problems, complex operating conditions such as parameter perturbation and external perturbations are taken into account. This paper proposes the third-order fast super-twisting (ST) non-singular fast terminal sliding mode control (NFTSMC) method based on an improved cubature Kalman filter (ICKF) without a speed sensor for IPMSM. The algorithm improves the third-order super-twisting by adding a linear term [15] and combines it with NFTSM to form a speed controller. At the same time, the non-singular terminal sliding mode is selected, and a double power convergence law is introduced to design IESMDO to accurately estimate the unknown partial disturbances in real-time and to compensate the INFTSMC with feedforward. By designing ICKF to estimate the rotor position and speed of the motor, the IPMSM speed control system without a speed sensor is constituted, which effectively improves the anti-interference capability and robustness of the motor closed-loop control system.

2. MATHEMATICAL MODEL OF IPMSM

The IPMSM operates in the ideal state, and the stator voltage equation in the *d-q* axis can be expressed as [16]:

$$\begin{cases} u_d = R_s i_d + L_d \dfrac{di_d}{dt} - \omega_e L_q i_q \\ u_q = R_s i_q + L_q \dfrac{di_q}{dt} + \omega_e \left(L_d i_d + \psi_f\right) \end{cases} \tag{1}$$

where i_d and i_q are the stator *d-q* axis current components, respectively (A); u_d and u_q are the stator *d-q* axis voltage components, respectively (V); L_d and L_q are the stator winding *d-q* axis inductances, respectively (H); ψ_f is the permanent magnet chain (Wb); R_s is the stator resistance (Ω); ω_e is the electric angular velocity (rad/s).

The IPMSM electromagnetic torque equation can be expressed as:

$$T_e = \frac{3}{2} n_p \left[\psi_f + \left(L_d - L_q\right) i_d\right] i_q = \frac{3}{2} n_p \psi_{ext} i_q \tag{2}$$

where T_e is the electromagnetic torque output by IPMSM ($N \cdot m$); $\psi_{ext} = \psi_f + (L_d - L_q) i_d$, ψ_{ext} is the effective magnetic chain; n_p is the number of pole pairs.

The mechanical motion equation of IPMSM can be expressed as:

$$\frac{d\omega_e}{dt} = \frac{n_p}{J} \left(T_e - T_L - B\omega_m\right) \tag{3}$$

where T_L is the load torque ($\mathrm{N} \cdot \mathrm{m}$); J is the moment of inertia ($\mathrm{kg} \cdot \mathrm{m}^2$); B is the damping coefficient ($\mathrm{N} \cdot \mathrm{m} \cdot \mathrm{s}$); ω_m is the mechanical angular speed of the motor (rad/s).

Considering the impact of IPMSM operation on system stability under complex conditions, the

mathematical model of IPMSM can be further obtained as [17]:

$$\begin{cases} u_d = R_s i_d + L_d \dfrac{di_d}{dt} - \omega_e L_q i_q + \Delta u_d \\ u_q = R_s i_q + L_q \dfrac{di_q}{dt} + \omega_e (L_d i_d + \psi_f) + \Delta u_q \\ T_e = \dfrac{3}{2} n_p \psi_{ext} i_q + \Delta T_e \end{cases} \tag{4}$$

where Δu_d and Δu_q are the d-q axis voltage perturbations caused by parameter uptake, respectively (V); ΔT_e is the output electromagnetic torque perturbation ($\mathrm{N} \cdot \mathrm{m}$).

Substituting Eq. (4) into Eq. (3):

$$\frac{d\omega_e}{dt} = \frac{3n_p^2}{2J} \psi_{ext} i_q - \frac{B}{J} \omega_e - \frac{n_p}{J} (\Delta T_e - T_L + \Delta T_L) = \gamma i_q + \xi \omega_e + F \tag{5}$$

where $\gamma = 3n_p^2 \psi_{ext}/2J$; $\xi = -B/J$.

3. DESIGNED OF INFTSMC SPEED CONTROLLER BASED ON IESMDO

To ensure the high-performance control of IPMSM even under extreme conditions, this section improves the super-twisting by adding a linear term and combines with NFTSM, the INFTSM control strategy. This control method is used to design the IPMSM speed controller, in which the third-order fast super-twisting control law solves the problems of slow convergence and parameter range limitations of traditional super-twisting.

3.1. Designed of INFTSMC Speed Controller

From Eq. (5), the control law of the speed controller can be designed as [18]:

$$i_q^* = \frac{\dot{\omega}_e^* - \xi \omega_e - F + u_c}{\gamma} \tag{6}$$

where i_q^* is the given q-axis current component; ω_e^* is the given speed of the system; u_c is the control output of INFTSMC.

Substituting Eq. (5) into Eq. (6):

$$\dot{\omega}_e^* - \dot{\omega}_e + u_c = 0 \tag{7}$$

The state error of the controller e is defined as $e = \omega_e^* - \omega_e$. The equation of state is given by $\dot{e}_1 = e_2$, $\dot{e}_2 = \dot{e}$. The NFTSM surface was chosen as [19]:

$$s = e_1 + \alpha e_1^{g/h} + \beta e_2^{p/q} \tag{8}$$

where $\alpha > 0$; $\beta > 0$; $g > 0$, $h > 0$, $p > 0$, $q > 0$, $1 < p/q < 2$; $g/h > p/q$.

Taking the derivative of Eq. (8):

$$\dot{s} = \dot{e}_1 + \alpha \frac{g}{h} e_1^{g/h-1} e_2 + \beta \frac{p}{q} e_2^{p/q-1} \dot{e}_2 = e_2 + \alpha \frac{g}{h} e_1^{g/h-1} e_2 + \beta \frac{p}{q} e_2^{p/q-1} \dot{e}_2 \tag{9}$$

The traditional ST expression can be expressed as [15]:

$$\begin{cases} \dot{s} = -l_1 |s|^{\frac{1}{2}} \operatorname{sgn}(s) + g \\ \dot{g} = -l_2 \operatorname{sgn}(s) \end{cases} \tag{10}$$

where $l_1 > 0$; $l_2 > 0$. Under external perturbation, conventional ST finite-time convergence requires coefficients that satisfy the following values [15]:

$$\begin{cases} l_2 > L \\ l_1 > 2\sqrt{l_2 - \sqrt{l_2^2 - L^2}} \end{cases} \tag{11}$$

where L is the boundary of perturbation.

From Eq. (11), the finite values of l_1 and l_2 reduce the tunability of the system, and the absence of linear term in the conventional ST algorithm leads to too slow convergence of the sliding mode surface when it is far from the equilibrium point. The exponent of the state vector is always 1/2 which does not allow the state of the sliding mode surface system to converge to a smaller size. To make the state variables of the control system enter the sliding mode quickly, a linear term is added. The product of the two nonlinear terms is set to be a linear term, so that its exponent is adjustable, which enhances the tunability of the system. The improved super-twisting algorithm can be expressed as [15]:

$$\begin{cases} \dot{s} = -l_1\varphi_1(s) + g - l_1 s \\ \dot{g} = -l_2 f_2(s) \end{cases} \tag{12}$$

where

$$\varphi_1(s) = k_1 s + k_2 |s|^{\alpha} \operatorname{sgn}(s) + k_3 |s|^{1-\alpha} \operatorname{sgn}(s);$$

$$f_2(s) = (\varphi_1(s) + s)'(\varphi_1(s) + s) = \begin{bmatrix} (k_1+1)^2 s + k_2^2 a |s|^{2a-1} \operatorname{sgn}(s) + k_3^2(1-a)|s|^{1-2a}\operatorname{sgn}(s) + \\ (a+1)(k_1+1)k_2|s|^{a}\operatorname{sgn}(s) + k_2k_3\operatorname{sgn}(s) + (2-a)|s|^{1-a}\operatorname{sgn}(s) \end{bmatrix}.$$

Theorem 1: From Eq. (8) to Eq. (12), the INFTSMC feedback control law is designed as in Eq. (13) [18]:

$$u_c = \frac{q}{\beta p} e_2^{2-p/q} \cdot \left(1 + \frac{\alpha g}{h} e_1^{g/h-1}\right) + l_1\varphi_1(s) + l_2\varphi_2(s) + l_1 s \tag{13}$$

and Eq. (12) satisfies the condition of Eq. (14), then the state error e will converge in finite time $t_s \le \frac{2}{\gamma_1} \ln\left(1 + \frac{\gamma_1}{\gamma_2} V_1^{\frac{1}{2}}(0)\right)$.

$$\begin{cases} r_1 = k_1 \lambda_{\min}(\mathbf{Q}) / \lambda_{\max}(\mathbf{P}) \\ r_2 = k_2 k_3 \lambda_{\min}(\mathbf{Q}) \lambda_{\min}^{1/2}(\mathbf{P}) / \lambda_{\max}(\mathbf{P}) \end{cases} \tag{14}$$

Proof 1: The following Lyapunov function V is selected as:

$$V = \frac{1}{2} e_1^2 \tag{15}$$

Taking the derivative of V:

$$\dot{V} = e_1\dot{e}_1 = \upsilon(2V)^{q/p} \cdot e_1^{1-q/p} \cdot \left(1 + \alpha e_1^{g/h-1}\right)^{q/p} \tag{16}$$

where $1 - q/p$ and $g/h - 1$ are positive even numbers, so $\dot{V} \le 0$. From the Lyapunov stability theorem, the origin is in a globally stable state. The next step is to prove the time t_s for stable convergence of the improved fast ST control law on the sliding mode surface.

Eq. (12) is rewritten as:

$$\dot{s} = -l_1(\varphi_1(s) + s) - l_2 f_2(s) = -l_1 f_1(s) - l_2 f_2(s) \tag{17}$$

where $f_1(s) = (k_1+1)s + k_2|s|^{a}\operatorname{sgn}(s) + k_3|s|^{1-a}\operatorname{sgn}(s)$; $f_2(s) = f_1'(s)f_1(s)$.

Proof 2: The quadratic-like positive definite Lyapunov function $V(x)$ is selected as:

$$V(x) = \boldsymbol{\zeta}^{\mathrm{T}} \mathbf{P} \boldsymbol{\zeta} \tag{18}$$

where $\boldsymbol{\zeta}^{\mathrm{T}} = [\ f_1(s) \quad g\ ]$. It is easy to prove that $V(x)$ is a positive definite and continuous function.

Taking the derivative of $\boldsymbol{\zeta}$:

$$\dot{\boldsymbol{\zeta}} = [\ f_1'(s)\dot{s} \quad \dot{g}\ ]^{\mathrm{T}} = f_1'(s)[\ -l_1 f_1(s) + g \quad -l_2 f_1(s)\ ]^{\mathrm{T}} = f_1'(s) \begin{bmatrix} -l_1 & 1 \\ -l_2 & 0 \end{bmatrix} \begin{bmatrix} f_1(s) \\ \dot{g} \end{bmatrix} = f_1'(s)\mathbf{A}\boldsymbol{\zeta} \tag{19}$$

where $\mathbf{A} = \begin{bmatrix} -l_1 & 1 \\ -l_2 & 0 \end{bmatrix}$; $l_1 > 0$; $l_2 > 0$. The matrix $\mathbf{A}$ is a Hurwitz matrix.

For any positive definite symmetric matrix $\mathbf{Q}$, there must exist a positive definite symmetric matrix $\mathbf{P}$ satisfying the Lyapunov function $V(x)$.

$$\mathbf{A}^{\mathrm{T}}\mathbf{P}+\mathbf{P}\mathbf{A}=-\mathbf{Q} \tag{20}$$

Taking the derivative of Eq. (18):

$$\dot{V}(x)=\dot{\boldsymbol{\zeta}}^{\mathrm{T}}\mathbf{P}\boldsymbol{\zeta}+\boldsymbol{\zeta}^{\mathrm{T}}\mathbf{P}\dot{\boldsymbol{\zeta}}=f_1'(s)\,\boldsymbol{\zeta}^{\mathrm{T}}\left(\mathbf{A}^{\mathrm{T}}\mathbf{P}+\mathbf{P}\mathbf{A}\right)\boldsymbol{\zeta}=-f_1'(s)\,\boldsymbol{\zeta}^{\mathrm{T}}\mathbf{Q}\boldsymbol{\zeta} \tag{21}$$

where $f_1'(s)=(k_1+1)+k_2a\,|s|^{a-1}+k_3(1-a)\,|s|^{-a}>0$, $\dot{V}(x)$ is negatively fixed, and the system is asymptotically stable on a large scale.

From Eq. (18) and Eq. (21):

$$\lambda_{\min}(\mathbf{P})\,\|\boldsymbol{\zeta}\|_2^2\le V\le\lambda_{\max}(\mathbf{P})\,\|\boldsymbol{\zeta}\|_2^2 \tag{22}$$

where $\lambda_{\min}(\mathbf{P})\,\|\boldsymbol{\zeta}\|_2^2$ and $\lambda_{\max}(\mathbf{P})\,\|\boldsymbol{\zeta}\|_2^2$ are the minimum and maximum eigenvalues of the matrix $\mathbf{P}$; $\|\boldsymbol{\zeta}\|_2^2$ is the 2-norm on Euclidean space $\mathbf{R}^2$, as shown in Eq. (23):

$$\begin{aligned}\|\boldsymbol{\zeta}\|_2^2&=\zeta_1^2+\zeta_2^2=f_1^2(s)+g^2\\&=(k_1+1)^2s^2+k_2^2\,|s|^{2a}+k_3^2\,|s|^{2-2a}+2(k_1+1)k_2\,|s|^{a+1}+2(k_1+1)k_3\,|s|^{2-a}+2k_2k_3\,|s|+g^2\end{aligned} \tag{23}$$

From Eq. (22) and Eq. (23):

$$\begin{cases}k_2\,|s|^a\le\|\boldsymbol{\zeta}\|_2\le\left(V(x)/\lambda_{\min}(\mathbf{P})\right)^{1/2}\\k_3\,|s|^{1-a}\le\|\boldsymbol{\zeta}\|_2\le\left(V(x)/\lambda_{\min}(\mathbf{P})\right)^{1/2}\end{cases} \tag{24}$$

From Eq. (21) and Eq. (24):

$$\begin{aligned}\dot{V}(x)&=-f_1'(s)\,\boldsymbol{\zeta}^{\mathrm{T}}\mathbf{Q}\boldsymbol{\zeta}\\&\le-\lambda_{\min}(\mathbf{Q})\,f_1'(s)\,\|\boldsymbol{\zeta}\|_2^2-k_2a\lambda_{\min}(\mathbf{Q})\,|s|^{a-1}\,\|\boldsymbol{\zeta}\|_2^2-k_3(1-a)\lambda_{\min}(\mathbf{Q})\,|s|^{-a}\,\|\boldsymbol{\zeta}\|_2^2\\&\le-\frac{(k_1+1)\lambda_{\min}(\mathbf{Q})}{\lambda_{\max}(\mathbf{P})}V-\frac{k_2a\lambda_{\min}(\mathbf{Q})}{\lambda_{\max}(\mathbf{P})}V\frac{1}{|s|^{1-a}}-\frac{k_3(1-a)\lambda_{\min}(\mathbf{Q})}{\lambda_{\max}(\mathbf{P})}V\frac{1}{|s|^a}\\&=-\frac{(k_1+1)\lambda_{\min}(\mathbf{Q})}{\lambda_{\max}(\mathbf{P})}V-\frac{k_2k_3\lambda_{\min}(\mathbf{Q})\,\lambda_{\min}^{1/2}(\mathbf{P})}{\lambda_{\max}(\mathbf{P})}V^{1/2}=-r_1V-r_2V^{1/2}\end{aligned} \tag{25}$$

where $r_1=(k_1+1)\lambda_{\min}(\mathbf{Q})/\lambda_{\max}(\mathbf{P})$; $r_2=k_2k_3\lambda_{\min}(\mathbf{Q})\lambda_{\min}^{1/2}(\mathbf{P})/\lambda_{\max}(\mathbf{P})$.

Eq. (25) is rewritten as:

$$\left(\frac{1}{2}\cdot V^{-1/2}\cdot\dot{V}\right)+\frac{r_1}{2}\left(V^{1/2}\right)=-\frac{r_2}{2} \tag{26}$$

Eq. (26) is equivalent to Eq. (27):

$$\left(V^{1/2}\right)'+\frac{r_1}{2}\left(V^{1/2}\right)=-\frac{r_2}{2} \tag{27}$$

Solving Eq. (27):

$$V^{\frac{1}{2}}=-\frac{r_2}{r_1}+\frac{r_2}{r_1}\cdot\exp^{-\frac{r_1}{2}t}+V^{\frac{1}{2}}(0)\cdot\exp^{-\frac{r_1}{2}t} \tag{28}$$

The stable convergence time of the improved super-twisting control law on the sliding mode surface t_s can be obtained from Eq. (29):

$$t_s\le\frac{2}{r_1}\ln\left(1+\frac{r_1}{r_2}V^{\frac{1}{2}}(0)\right) \tag{29}$$

where when $r_1=0$ or $r_2=0$, $V(x)$ is a simple exponential convergence, and e will converge in a finite time.

When the sliding mode surface converges in finite time, that is $s=\dot{s}=0$, the equivalent control law can be obtained as:

$$u_c=\frac{q}{\beta p}\,e_2^{2-p/q}\cdot\left(1+\frac{\alpha g}{h}\,e_1^{g/h-1}\right)+l_1\varphi_1(s)+l_2\varphi_2(s)+l_1s \tag{30}$$

Substituting Eq. (30) into Eq. (6) to obtain i_q^* as:

$$i_q^* = \frac{\dot{\omega}_e^* - \xi\omega_e - F + u_c}{\gamma} \frac{\dot{\omega}_e^* - \xi\omega_e - F + \dfrac{q}{\beta p} e_2^{2-p/q} \cdot \left(1 + \dfrac{\alpha g}{h} e_1^{g/h-1}\right) + l_1\varphi_1(s) + l_2\varphi_2(s) + l_1 s}{\gamma} \tag{31}$$

Fig. 1 is the block diagram of the INFTSMC.

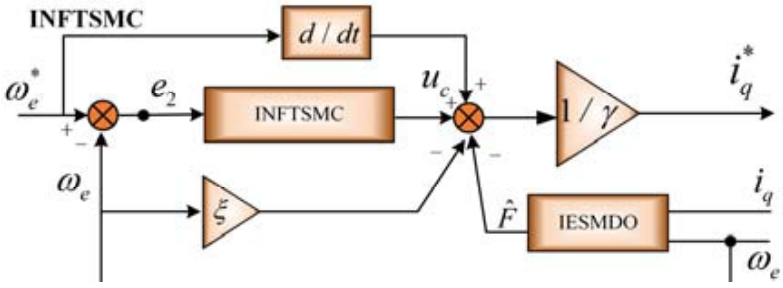

Figure 1. The block diagram of INFTSMC.

3.2. Designed of Improved Extended Sliding Mode Disturbance Observer (IESMDO)

Based on the conventional sliding mode perturbation observer (SMO), the non-singular terminal is selected as the sliding mode surface to effectively reduce the convergence time of the system, improving the jitter caused by the high gain of the conventional SMO and enhancing the performance of the observer for speed tracking by introducing a double power convergence law.

Defining variable as $x_1 = \hat{\omega}_e - \omega_e$, Eq. (6) is redefined as:

$$\begin{cases} \dfrac{d\hat{\omega}_e}{dt} = \gamma i_q + \xi\hat{\omega}_e + \hat{F} + u_{smo} \\ \dfrac{d\tilde{F}}{dt} = G \cdot u_{smo} \end{cases} \tag{32}$$

where $\hat{\omega}_e$ is the observed speed; $\hat{F}$ is the estimated value of F; u_{smo} is the control law of IESMDO.

From Eq. (5) and Eq. (32), Eq. (33) can be obtained as:

$$\begin{cases} \dot{x}_1 = \xi x_1 + \tilde{F} + u_{smo} \\ \dfrac{d\tilde{F}}{dt} = G \cdot u_{smo} - \ell(t) \end{cases} \tag{33}$$

where $\tilde{F} = \hat{F} - F$; $\ell(t) = dF/dt$.

Selecting NTSM surface [20]:

$$s_1 = x_1 + c_1 \dot{x}_1^{g/t} \tag{34}$$

where $c_1 > 0$; g and t are the positive odd numbers to be designed; $1 < g/t < 2$.

Taking the derivative of Eq. (34):

$$\dot{s}_1 = \dot{x}_1 + c_1 \frac{g}{t} \dot{x}_1^{g/t-1} \ddot{x}_1 \tag{35}$$

The double power convergence law is designed [21]:

$$\dot{s}_1 = -\tau_1 |s_1|^{b_1} \operatorname{sgn}(s_1) - \tau_2 |s_1|^{b_2} \operatorname{sgn}(s_1) \tag{36}$$

where τ_1 and τ_2 are the positive odd numbers to be designed; $b_1 = 1 - r$; $b_2 = 1 + r$; $0 < r < 1$.

From Eqs. (34)$\sim$(36), u_{smo} can be obtained as:

$$u_{smo} = u_{eq} + u_{fn} \tag{37}$$

where $u_{eq} = -\xi x_1$; $u_{fn} = -\int_0^t \left(\frac{t}{c_1 g}\dot{x}_1^{2-g/t} + \tau_1 |s_1|^{b_1} \operatorname{sgn}(s_1) + \tau_2 |s_1|^{b_2} \operatorname{sgn}(s_1)\right) d\tau$.

Theorem 2: From Eq. (32) to Eq. (37), when the gains are chosen to satisfy Eq. (39), x_1 converges to 0 in finite time [18].

$$\begin{cases} \tau_1 |s_1|^{b_1+1} \geq \left|\dot{\tilde{F}}\right| \\ \tau_2 |s_1|^{b_2+1} \geq \left|\dot{\tilde{F}}\right| \end{cases} \tag{38}$$

Proof 3: The following Lyapunov function V_1 is selected as:

$$V_1 = \frac{1}{2} s_1^2 \tag{39}$$

Taking the derivative of V_1:

$$\dot{V}_1 = s_1 \dot{s}_1 = s_1 \left(\dot{x}_1 + c_1 \frac{g}{t} \dot{x}_1^{g/t-1} \ddot{x}_1\right) = s_1 \cdot c_1 \frac{g}{t} \dot{x}_1^{g/t-1} \left(\ddot{x}_1 + \frac{t}{c_1 g} \dot{x}_1^{2-g/t}\right) \tag{40}$$

Substituting Eq. (37) into Eq. (33):

$$\dot{x}_1 = \tilde{F} + u_{fn} \tag{41}$$

Taking the derivative of Eq. (41):

$$\ddot{x}_1 = \dot{\tilde{F}} + \dot{u}_{fn} \tag{42}$$

From Eq. (37)∼Eq. (43):

$$\begin{aligned} \dot{V}_1 &= s_1 \cdot \frac{c_1 g}{t} \dot{x}_1^{g/t-1} \left(\dot{\tilde{F}} - \tau_1 |s_1|^{b_1} \operatorname{sgn}(s_1) - \tau_2 |s_1|^{b_2} \operatorname{sgn}(s_1)\right) \\ &= -\frac{c_1 g}{t} \dot{x}_1^{g/t-1} \left(-s_1 \cdot \dot{\tilde{F}} + \tau_1 |s_1|^{b_1} \operatorname{sgn}(s_1) \cdot s_1 + \tau_2 |s_1|^{b_2} \operatorname{sgn}(s_1) \cdot s_1\right) \\ &= -\frac{c_1 g}{t} \dot{x}_1^{g/t-1} \left(-s_1 \cdot \dot{\tilde{F}} + \tau_1 |s_1|^{b_1+1} + \tau_2 |s_1|^{b_2+1}\right) \end{aligned} \tag{43}$$

Because of $g/t > 0$, $\dot{x}_1^{g/t-1} > 0$, Eq. (43) can be transformed into two forms:

$$\begin{aligned} \dot{V}_1 &= -\frac{c_1 g}{t} \dot{x}_1^{g/t-1} \left(-s_1 \cdot \dot{\tilde{F}} + \tau_1 |s_1|^{b_1+1} + \tau_2 |s_1|^{b_2+1}\right) \\ &\leq -\frac{c_1 g}{t} \dot{x}_1^{g/t-1} \left(\tau_1 |s_1|^{b_1+1} + |s_1| \left(\tau_2 |s_1|^{b_2+1} - |\dot{\tilde{F}}|\right)\right) \end{aligned} \tag{44}$$

$$\begin{aligned} \dot{V}_1 &= -\frac{c_1 g}{t} \dot{x}_1^{g/t-1} \left(-s_1 \cdot \dot{\tilde{F}} + \tau_1 |s_1|^{b_1+1} + \tau_2 |s_1|^{b_2+1}\right) \\ &\leq -\frac{c_1 g}{t} \dot{x}_1^{g/t-1} \left(\tau_2 |s_1|^{b_2+1} + |s_1| \left(\tau_1 |s_1|^{b_2+1} - |\dot{\tilde{F}}|\right)\right) \end{aligned} \tag{45}$$

If $\left|\dot{\tilde{F}}\right| \leq N$, $N \geq 0$, when $\tau_2 |s_1|^{b_2+1} \geq \left|\dot{\tilde{F}}\right|$:

$$\dot{V}_1 \leq -\frac{c_1 g}{t} \dot{x}_1^{g/t-1} \left(\tau_1 |s_1|^{b_1+1}\right) = -\frac{c_1 g}{t} \dot{x}_1^{g/t-1} \left(\tau_1 \cdot (2V_1)^{\frac{b_1+1}{2}}\right) \leq 0 \tag{46}$$

when $\tau_1 |s_1|^{b_1+1} \geq \left|\dot{\tilde{F}}\right|$:

$$\dot{V}_1 \leq -\frac{c_1 g}{t} \dot{x}_1^{g/t-1} \left(\tau_2 |s_1|^{b_2+1}\right) = -\frac{c_1 g}{t} \dot{x}_1^{g/t-1} \left(\tau_2 \cdot (2V_1)^{\frac{b_2+1}{2}}\right) \leq 0 \tag{47}$$

According to the Lyapunov stability theorem [20], it is known that the system will satisfy the sliding mode reachability condition.

From Eq. (46) and Eq. (47):

$$\begin{cases} |s_1| \leq \left(\dfrac{N}{\tau_2}\right)^{\frac{1}{b_2}} \\ |s_1| \leq \left(\dfrac{N}{\tau_1}\right)^{\frac{1}{b_1}} \end{cases} \tag{48}$$

From Eq. (48), the convergence region of s_1 can be found as:

$$|s_1| \leq \min\left(\left(\frac{N}{\tau_2}\right)^{\frac{1}{b_2}}, \left(\frac{N}{\tau_1}\right)^{\frac{1}{b_1}}\right) \tag{49}$$

Eq. (36) can be found as:

$$|\dot{s}_1| \leq \tau_1 |s_1|^{b_1} + \tau_2 |s_1|^{b_2} \leq \tau_1 \cdot \min\left(\left(\frac{N}{\tau_2}\right)^{\frac{1}{b_2}}, \left(\frac{N}{\tau_1}\right)^{\frac{1}{b_1}}\right)^{b_1} + \tau_2 \cdot \min\left(\left(\frac{N}{\tau_2}\right)^{\frac{1}{b_2}}, \left(\frac{N}{\tau_1}\right)^{\frac{1}{b_1}}\right)^{b_2} \tag{50}$$

Suppose that t_r is the convergence time of the s_1 from the initial value to $s_1 = 0$. The system enters the terminal sliding mode surface after post t_r and converges to 0 after t_e. The total convergence time can be expressed as [20]:

$$t = t_r + t_e = t_r + \frac{c_1 g}{g - t} \max\left(\left|x_1(t_r)^{1-g/t}\right|\right) \tag{51}$$

To effectively reduce the sliding mode jitter, the saturation function $\Re(s)$ is used instead of the sign function:

$$\Re(s) = \frac{2}{1 + \exp^{-\tau s}} \tag{52}$$

where $\tau > 0$. Fig. 2 is the block diagram of IESMDO.

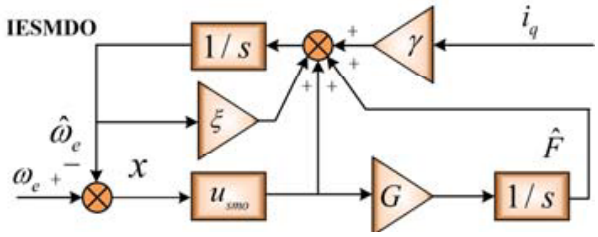

Figure 2. The block diagram of IESMDO.

4. DESIGNED OF IMPROVED SQUARE ROOT CUBATURE KALMAN-FILTER SENSORLESS (ICKF)

Considering the problems of high cost and strict environmental requirements of sensors, this section selects the high-order square root cubature Kalman algorithm. The speed and rotor position of the IPMSM are estimated by ICKF instead of an optical encoder, and it has good estimation accuracy.

4.1. State Equation of IPMSM

From Eq. (1) and Eq. (3), Eq. (53) can be expressed as:

$$\begin{cases} \dfrac{di_d}{dt} = \dfrac{1}{L_d}\left(u_d + n_p\omega_m L_q i_q - R_s i_d\right) \\ \dfrac{di_q}{dt} = \frac{1}{L_q}\left(u_q - n_p\omega_m L_d i_d - n_p\omega_m\psi_f - R_s i_q\right) \\ \dfrac{d\omega_m}{dt} = \dfrac{1}{J}\left(T_e - T_L - B\omega_m\right) \\ \dfrac{d\theta_m}{dt} = \omega_m \end{cases} \tag{53}$$

where ω_m is the mechanical angular velocity; θ_m is the mechanical angle.

Selecting the new state variable: $x^* = [\ i_d \quad i_q \quad \omega_m \quad \theta_m\ ]^T$; $u = [\ u_d \quad u_q \quad T_e \quad T_L\ ]^T$; $y = [\ i_d \quad i_q\ ]^T$.

Development of a nonlinear mathematical model of the motor:

$$\begin{cases} \dot{x}^*(t) = Ax(t) + Bu(t) + w \\ z(t) = Cx(t) + v \end{cases} \tag{54}$$

Discretizing the state equation, letting T be the sampling period:

$$\begin{cases} \dot{x}^*(k) = G_1 x(k-1) + Hu(k-1) + W_{k-1} \\ Z(k-1) = Cx(k-1) + v_{k-1} \end{cases} \tag{55}$$

4.2. Improved Square Root Cubature Kalman-Filter (ICKF)

Generalized fifth-order volume integral formula can be expressed as [22]:

$$I(g) = \int_{R^n} g(x)N(x;0,I)\mathrm{d}x = \hat{W}_0 g([0]) + \hat{W}_1 \sum_{2n}^{i=1} g([v]_i) + \hat{W}_{1,1} \sum_{2n(n-1)}^{i=1} g([v,v]_i) \tag{56}$$

where $\hat{W}_0$, $\hat{W}_1$, and $\hat{W}_{1,1}$ are the weights of the corresponding trajectories of $[0]$, $[v]_i$, and $[v,v]_i$, respectively; n is the number of system state dimensions; v needs to satisfy the following Eq. (57):

$$\begin{pmatrix} I_0 \\ I_2 \\ I_4 \\ I_{2,2} \end{pmatrix} = \begin{pmatrix} 1 & 2n & 2n(n-1) \\ 0 & 2v^2 & 4(n-1)v^2 \\ 0 & 2v^4 & 4(n-1)v^4 \\ 0 & 0 & 4v^4 \end{pmatrix} \begin{pmatrix} \hat{W}_0 \\ \hat{W}_1 \\ \hat{W}_{1,1} \end{pmatrix} \tag{57}$$

where $I_0 = \int_{R^n} \exp(-x^T x)\mathrm{d}x = \sqrt{\pi^n}$; $I_2 = \int_{R^n} x_i^2 \exp(-x^T x)\mathrm{d}x = \sqrt{\pi^n}/2$; $I_4 = \int_{R^n} x_i^4 \exp(-x^T x)\mathrm{d}x = 3\sqrt{\pi^n}/4$; $I_{2,2} = \int_{R^n} x_i^2 x_j^2 \exp(-x^T x)\mathrm{d}x = \sqrt{\pi^n}/4$.

According to Eq. (57), the solution can be found as:

$$\begin{cases} v = \sqrt{3/2} \\ \hat{W}_0 = \sqrt{\pi^n}\,(1 - (7-n)n/18) \\ \hat{W}_1 = \sqrt{\pi^n}\,[(4-n)/18] \\ \hat{W}_{1,1} = \sqrt{\pi^n}/36 \end{cases} \tag{58}$$

Convert Eq. (56) to the standard Gaussian distribution form:

$$\begin{aligned} I(g) &= \int_{R^n} g(x)N(x;0,I)\mathrm{d}x = \frac{1}{\sqrt{\pi^n}} \int_{R^n} g(\sqrt{2}x) \times \exp\left(-x^{\mathrm{T}}x\right)\mathrm{d}x \\ &= \left(1 - \frac{(7-n)n}{18}\right) g([0]) + \frac{4-n}{18} \sum_{2n}^{i=1} g\left([\sqrt{3}]_i\right) + \frac{1}{36} \sum_{2n(n-1)}^{i=1} g\left([\sqrt{3},\sqrt{3}]_i\right) = \sum_{2n^2+1}^{i=1} \omega_i g(\xi_i) \end{aligned} \tag{59}$$

From Eq. (59), volume points $\tilde{\xi}$ and weight $\tilde{\omega}_i$ can be expressed as [22]:

$$\xi_i = \begin{cases} [0]_i, & i = 1 \\ [\sqrt{3}]_i, & i = 2, \cdots, 2n+1 \\ [\sqrt{3},\sqrt{3}]_i, & i = 2n+2, \cdots, 2n^2+1 \end{cases} \tag{60}$$

$$\omega_i = \begin{cases} 1 - n(7-n)/18 & i = 1 \\ (4-n)/18 & i = 2, \cdots, 2n+1 \\ 1/36 & i = 2n+2, \cdots, 2n^2+1 \end{cases} \tag{61}$$

According to the Sage-Husa recursive estimation method [23], a time-varying noise statistical valuator is designed to estimate the variance $\tilde{R}_k$ of $v(k)$ in real-time:

$$\tilde{R}_k = (1 - d_{k-1})\tilde{R}_{k-1} + d_{k-1}\left(\tilde{z}_k\tilde{z}^{\mathrm{T}} - H_{k,k-1}P_{k|k-1}H_{k,k-1}^{\mathrm{T}}\right) \tag{62}$$

where $d_{k-1} = (1-b)/(1-b^k)$; b is the forgetting factor, $0.95 < b < 0.99$; $\tilde{z}_k = z_k - h(\hat{x}_{k|k-1})$ is the measurement of new news; $H_{k,k-1}$ is the linearized observation matrix.

Eq. (63) is designed according to the EKF equation:

$$P_{xz,k|k-1} = P_{k|k-1}H_{k,k-1}^{\mathrm{T}} \tag{63}$$

Substituting $P_{k|k-1} = S_{k|k-1}S_{k|k-1}^{T}$ into Eq. (63):

$$H_{k,k-1} = P_{xz,k|k-1}^{\mathrm{T}}/(S_{k|k-1}^{\mathrm{T}}S_{k|k-1}) \tag{64}$$

Substituting Eq. (63) and Eq. (64) into Eq. (62):

$$\hat{R}_k = (1 - d_{k-1})\hat{R}_{k-1} + d_{k-1}\left(\tilde{z}_k\tilde{z}^{\mathrm{T}} - P_{xz,k|k-1}^{\mathrm{T}}\left(S_{k|k-1}^{\mathrm{T}}S_{k|k-1}\right)^{-1}P_{xz,k|k-1}\right) \tag{65}$$

4.3. Algorithm-Specific Steps of ICKF

The algorithm process includes system initialization, state prediction, and state update. The specific formulas are derived as follows:

a) System initialization:

$$\begin{cases} \hat{x}_0 = E(x_0) \\ S_0 = \mathrm{chol}(p_0) \\ \hat{R}_0 = R_0 \end{cases}$$

where chol$(*)$ indicates the Cholesky decomposition; system initial state is $x_0 = [\ 0 \quad 0 \quad 0 \quad 0\ ]$; the initial state covariance array is $p_0 = [\ 0.5 \quad 0.5 \quad 0.01 \quad 0.0\ ]$; $R_0 = \mathrm{diag}[\ 0.1 \quad 0.1\ ]$.

b) Prediction process [23]:

(1) Calculating the higher order volume points ($i = 0, 1, ..., 2n^2$)

$$x_{i,k-1|k-1} = S_{k-1|k-1}\xi_i + \hat{x}_{k-1|k-1} \tag{66}$$

where $S_{k-1|k-1} = \mathrm{chol}(P_{k-1|k-1})$.

(2) Calculating the volume points after propagation

$$x_{i,k|k-1}^{*} = f\left(x_{i,k|k-1}\right) \tag{67}$$

where $x_{i,k|k-1}^{*}$ are the volume points of propagation in the prediction process.

(3) Stating prediction estimates

$$\hat{x}_{k|k-1} = \sum_{i=0}^{2n^2}\omega_i x_{i,k|k-1}^{*} \tag{68}$$

In Eq. (69), the predicted values of the state variables $\hat{x}_{k|k-1}$ are obtained by weighting and summing the propagated volume points $x_{i,k|k-1}^{*}$.

(4) Calculating the square roots of the prediction error variance array

$$S_{k|k-1} = qr\left[\sqrt{\omega_0}\left(x_{0,k|k-1}^{*} - \hat{x}_{k|k-1}\right)\cdots\sqrt{\omega_{2n^2}}\left(x_{2n^2,k|k-1}^{*} - \hat{x}_{k|k-1}\right)\sqrt{Q_{k-1}}\right] \tag{69}$$

where $qr(*)$ indicates the QR decomposition; $S_{k|k-1}$ are the square roots of the error variance array of the prediction process.

c) Update process:

When the predicted value at moment k is obtained, it is updated and corrected by the measurement equation and the gain matrix.

(1) Calculation of higher order volume points ($i = 0, 1, ..., 2n^2$)

$$x_{i,k|k-1} = S_{k|k-1}\xi_i + \hat{x}_{k|k-1} \tag{70}$$

(2) Calculating the volume points after propagation

$$z_{i,k|k-1} = h\left(x_{i,k|k-1}\right) \tag{71}$$

where $z_{i,k|k-1}$ are the volume points propagated during the measurement.

(3) Measurement state prediction

$$\hat{z}_{k|k-1} = \sum_{i=0}^{2n^2} \omega_i z_{i,k|k-1} \tag{72}$$

where the predicted value of the volume prediction $\hat{z}_{k|k-1}$ is obtained by weighting the sum of the volume points of the volume measurement equation $z_{i,k|k-1}$.

(4) Calculating the square roots of the new interest covariance array

$$S_{zz,k|k-1} = qr\left[\sqrt{\omega_0}\left(z_{0,k|k-1} - \hat{z}_{k|k-1}\right) \cdots \sqrt{\omega_{2n^2}}\left(z_{2n^2,k|k-1} - \hat{z}_{k|k-1}\right)\sqrt{\hat{R}_k}\right] \tag{73}$$

where $\sqrt{\hat{R}_k}$ is the Cholesky decomposition factor of the matrix $\hat{R}_k$; $S_{zz,k|k-1}$ is the quantitative measurement covariance array of the new rest at moment k.

(5) Calculating the mutual covariance array and gain array

$$\begin{cases} P_{xz,k|k-1} = \sum_{i=0}^{2n^2} \omega_i \left[x_{i,k|k-1} - \hat{x}_{k|k-1}\right] \times \left[z_{i,k|k-1} - \hat{z}_{k|k-1}\right]^{\mathrm{T}} \\ K_k = \left[P_{xz,k|k-1}/S_{zz,k|k-1}^{\mathrm{T}}\right]/S_{zz,k|k-1} \end{cases} \tag{74}$$

where K_k is the Kalman gain matrix at moment k; $P_{xz,k|k-1}$ is the measurement mutual covariance array at moment k.

(6) Estimating the square roots of the state and its covariance array

$$\begin{cases} \hat{x}_{k|k} = \hat{x}_{k|k-1} + K_k\left[z_k - \hat{z}_{k|k-1}\right] \\ S_{k|k} = \mathrm{chol} * \left[S_{k|k-1'}K_k S_{zz,k|k-1'} - 1\right] \end{cases} \tag{75}$$

where $\hat{x}_{k|k}$ is the state estimate at moment k; chol$*$ indicates a Cholesky update.

After correcting the predicted values to obtain the optimal estimates of the system state variables $\hat{x}_{k|k}$ at moment k and the square root of its covariance array $S_{k|k}$, then return to Eq. (66) for another state cycle.

5. EXPERIMENTS RESULTS

To verify the feasibility of the algorithm, the IESMDO based INFTSMC sensor-less algorithm is built in MATLAB platform. The parameters of IPMSM are shown in Table 1. Table 2 shows the control parameters. Fig. 3 is the block diagram of IPMSM.

Remark 1: The values of γ and ξ in the algorithm of this paper are rectified by $\gamma = 3n_p^2\psi_{ext}/2J$ and $\xi = -B/J$. The NFTSMC algorithm is $s = e_1 + \alpha_1 e_1^{g_1/h_1} + \beta_1 e_2^{p_1/q_1}$. The conventional ST control law $\dot{s} = -l_3\left|s\right|^{\frac{1}{2}}\mathrm{sgn}(s) - \int l_4 \mathrm{sgn}(s)d\tau$ is chosen, and NFTSMC controller selects the traditional SMO for the observation of system disturbance. Instead of the photoelectric encoder, the ICKF algorithm is selected for PI, NFTSMC, and INFTSMC algorithms to estimate the speed and position to form a closed-loop control.

From Fig. 3, the red dashed box shows the proposed algorithm in this paper, whose control flow is as follows: Firstly, designing the modified super-twisting non-singular fast terminal sliding mode controllers for the speed loop of IPMSM. At the same time, the IESMDO accurately observes, in real time, the external disturbance and parameters ingestion parts, and feeds the observed values into the controller to achieve stable operation of the IPMSM under complex operating conditions.

Table 1. The parameters of IPMSM.

Parameters	Units	Values
Dc voltage/u_{dc}	V	600
Rated speed/n_N	r/min	1900
Stator resistance/R_s	Ω	2.75
Pole number/n_p	pairs	2
d axis inductance/L_d	H	0.004
q axis inductance/L_q	H	0.009
Magnet flux/ψ_f	Wb	0.12
Inertia/J	kg · m^2	0.029

Table 2. The parameters of PI/NFTSMC/INFTSMC.

PI	NFTSMC	INFTSMC
$P = 100$	$\alpha_1 = 0.01$	$\alpha = 0.05$
$I = 20$	$\beta_1 = 0.005$	$\beta = 0.01$
/	$p_1/q_1 = 7/5$	$p/q = 7/5$
/	$g_1/h_1 = 5/3$	$g/h = 5/3$
/	$l_3 = 0.6$	$k_1 = 0.5$
/	$l_4 = 1.5$	$k_2 = 1.8$
/	/	$k_3 = 0.9$
/	/	$a = 1/2$

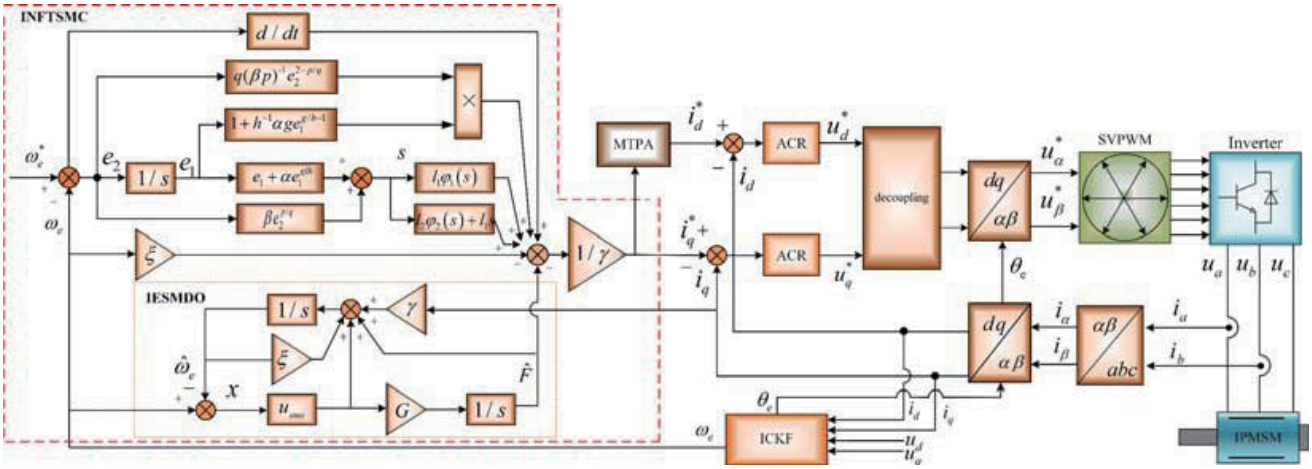

Figure 3. The block diagram of the motor speed control system.

5.1. Simulation Analysis of IPMSM under Parametric Uptake and Unknown Perturbation

The parameter regression experimental conditions are shown in Table 3.

Under the overall sensorless control, it can be seen from Fig. 4(a) that the response time of INFTSMC to reach the specified speed is smaller than PI and NFTSMC. In the motor system, the load variation has a large effect on the transient process of motor speed, while the resistance effect is

Table 3. Parameter perturbation experimental conditions.

Time	Perturbation	Range of perturbation
0.5 s	ψ_f/Wb	0.12→0.08
0.7 s	R_s/Ω	2.75→3.90
1.5 s	L_q/H	0.009→0.006
2.0 s	L_q/H	0.004→0.003
2.5 s	T_L/N·m	15→20

small and negligible. When the mechanical parameters of the motor are ingested, the speed of PI and NFTSMC control has significant fluctuation and overshoot, while the speed under INFTSMC control can accurately track to the given speed in a very short time. Fig. 4(a) shows that the steady-state control accuracy of INFTSMC is better than that of PI and NFTSMC in the enlarged plot for each operating condition. Figs. 4(b), (c), and (d) show that the INFTSMC has more stable torque and d-q axis current waveforms, better control performance in both transient and steady states, and minimal pulsation.

In Fig. 5(a), the SMO has some overshoot in the speed tracking due to the high gains when the motor parameters are regenerated, and some jitter occurs during the transient process. Compared with SMO, IESMDO has better speed tracking performance, improves the jitter caused by high gains of SMO, and effectively reduces the system convergence time by selecting non-singular terminals as the sliding mode surface and introducing the double power convergence law. From Fig. 5(b), the unknown perturbed part F waveform observed by IESMDO is smoother, and the jitter is effectively reduced.

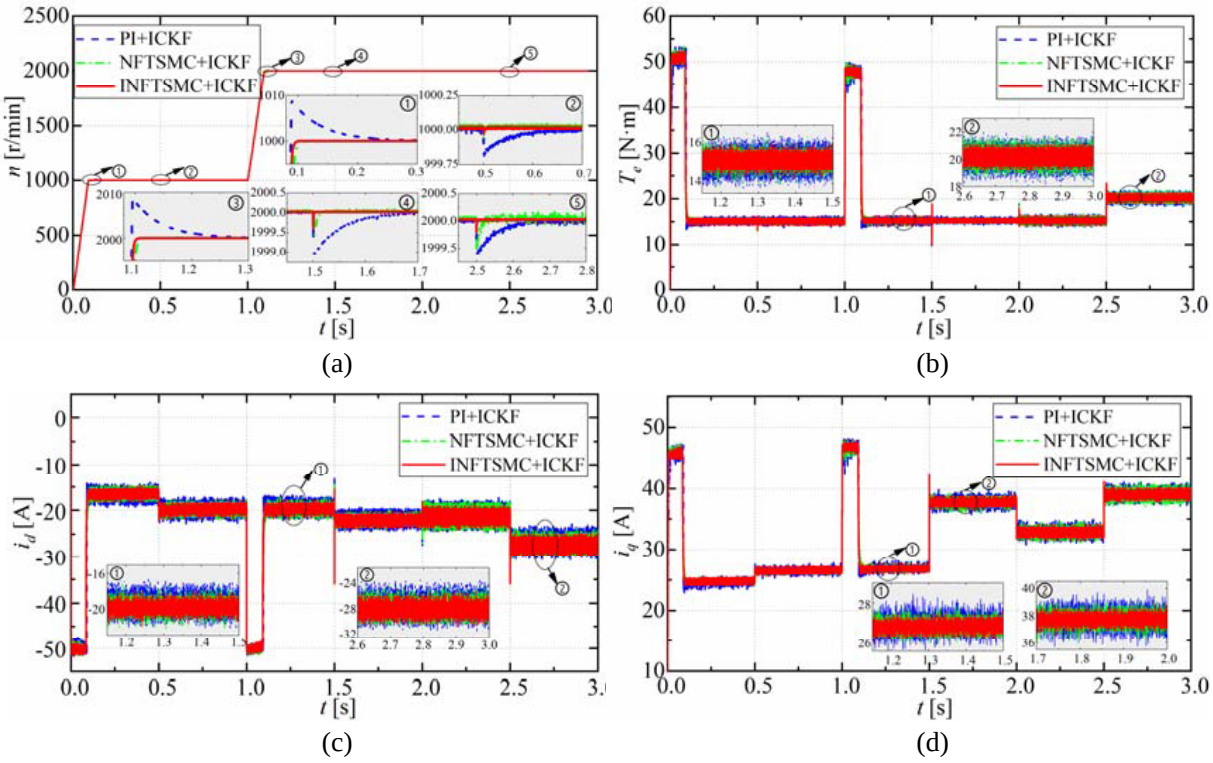

Figure 4. Simulation comparison results of PI+ICKF/NFTSMC+ICKF/INFTSMC+ICKF. (a) Simulation comparison of speed. (b) Simulation comparison of torque. (c) Simulation comparison of d-axis current. (d) Simulation comparison of q-axis current.

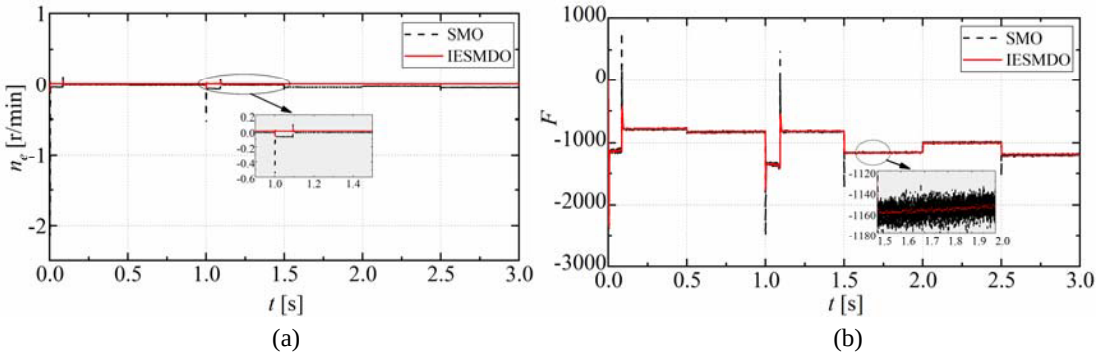

Figure 5. Simulation comparison results of SMO/IESMDO. (a) Speed tracking error e. (b) Unknown parts of the total perturbation F.

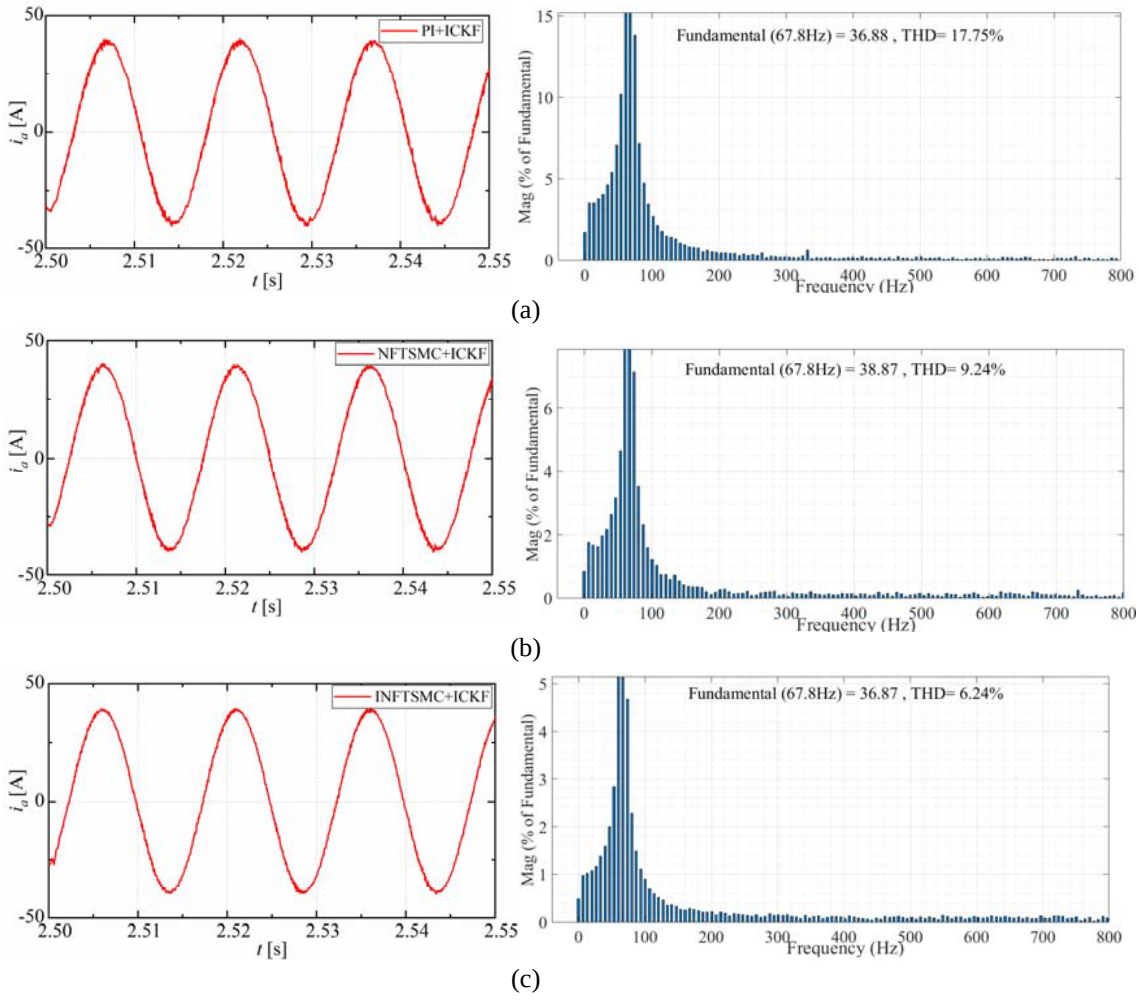

Figure 6. THD analysis of A phase stator current. (a) PI+ICKF. (b) NFTSMC+ICKF. (c) INFTSMC+ICKF.

From Fig. 6, Compared with the other two algorithms, the proposed INFTSMC+ICKF can effectively suppress current harmonics in the case of parameter ingestion. Table 4 shows the comprehensive performance comparison of PI, NFTSMC, and INFTSMC control methods under the ICKF closed loop.

Table 4. Comparison of PI+ICKF/NFTSMC+ICKF/INFTSMC+ICKF.

Performance indicators	PI+ICKF	NFTSMC+ICKF	INFTSMC+ICKF
Speed convergence time[1]	0.31/0.31	0.14/0.16	0.10/0.10
Torque ripple	14.52%	9.67%	5.11%
Speed static difference[2]	0.09/0.17	0.06/0.11	0.021/0.024
Average speed error rate[3]	0.0662	0.0321	0.011
i_a THD	17.75%	9.24%	6.24%

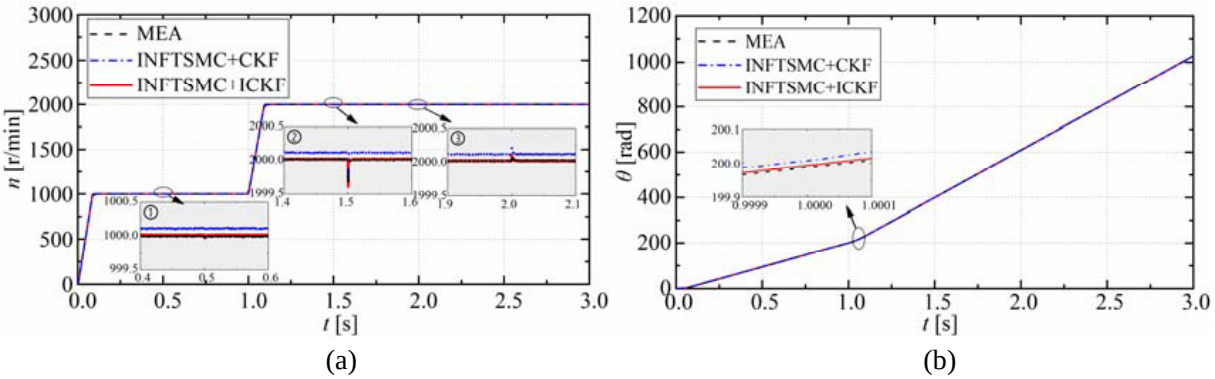

Figure 7. Combined simulation results of INFTSMC+ICKF. (a) Rotational speed estimation of INFTSMC+ICKF. (b) Rotor angle estimation of INFTSMC+ICKF.

Figure 7 shows the simulation comparison of the speed control system combining INFTSMC and ICKF. Fig. 7(a) is the speed estimation curve; Fig. 7(b) is the rotor angle estimation curve. (MEA is the measured value; CKF is the cubature Kalman-filter estimated value; and ICKF is the cubature Kalman-filter estimated value).

From Fig. 7, compared with the CKF, the ICKF algorithm for motor speed estimation slowly converges to the true value, and the maximum tracking speed relative errors at steady state are 0.005 and 0.001%, respectively. The speed estimation accuracy is higher than the common CKF algorithm in the speed regulation condition. When the load torque changes, the ICKF speed estimation error becomes a little larger, but still converges to the true value and estimates the motor speed more consistently than the CKF in the regenerated case. In summary, it can be seen that the ICKF algorithm has high estimation accuracy and is more adaptable. Table 5 shows the comparison of the speed and position estimation results of CKF and ICKF in the INFTSMC.

Table 5. The comparison of the speed and position estimation results of CKF and ICKF.

Performance Indicators	CKF	ICKF
Variance of speed error	0.143	0.046
Variance of position error	0.00041	0.00021

5.2. Analysis of RT-Lab Experimental Results

To further verify the effectiveness of the method, RT-Lab is used to implement the hardware-in-the-loop simulation (HILS) experiment of the IPMSM drive system. Fig. 8 is the RT-Lab experimental platform. Fig. 9 is the experimental plots of the full working conditions. From Fig. 8, RT-LAB (OP5600) is used

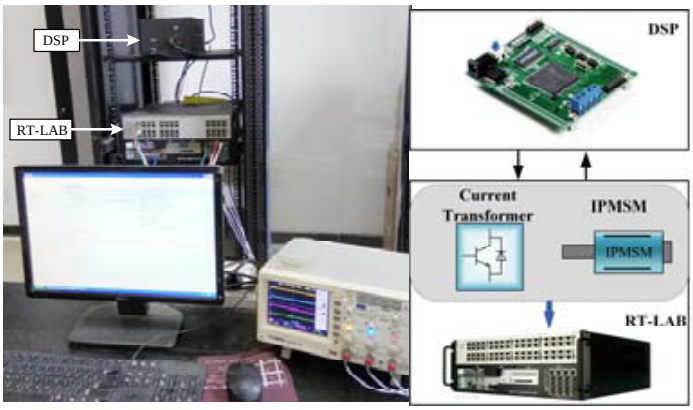

Figure 8. RT-LAB experimental platform.

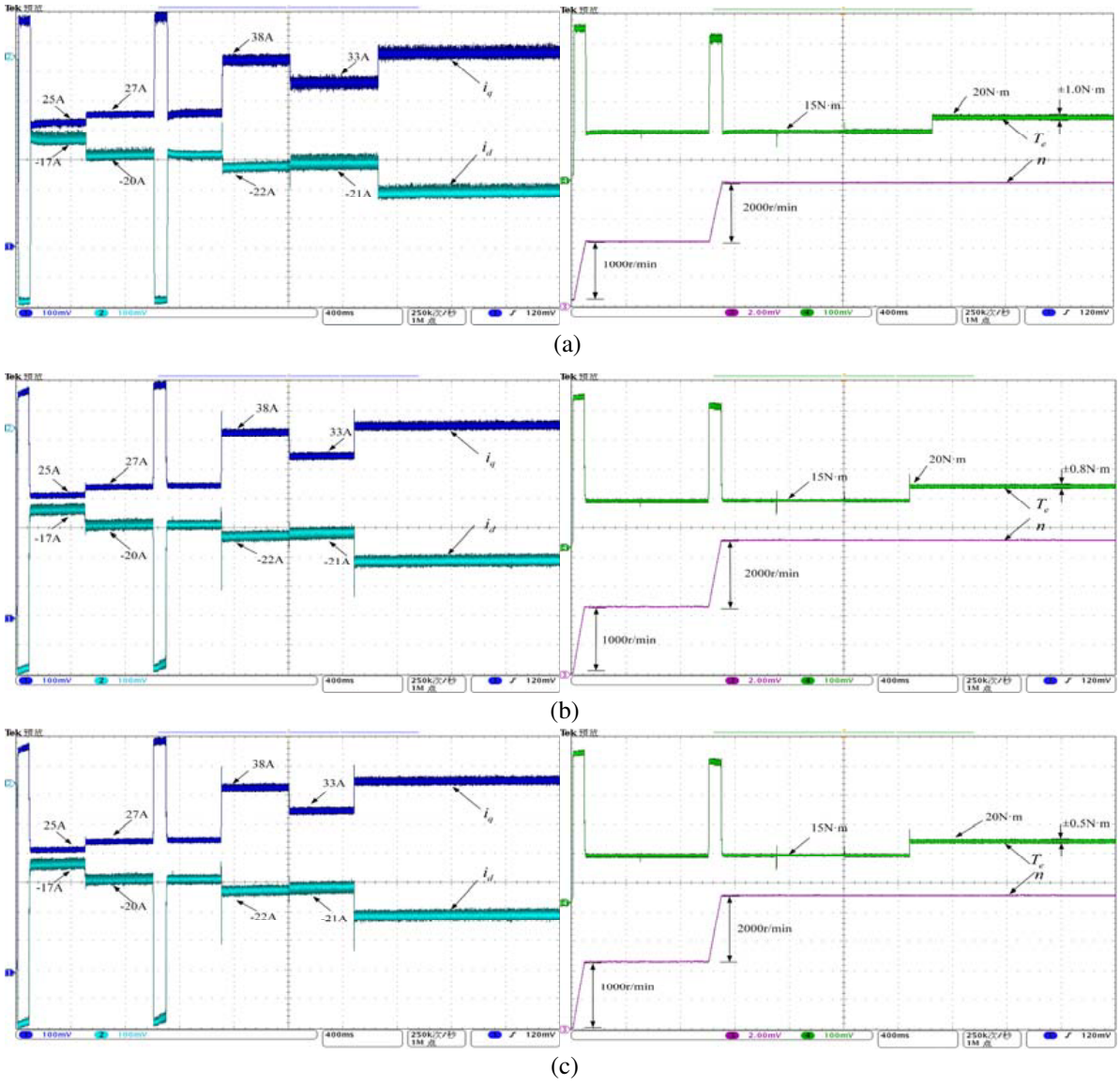

Figure 9. Comparison of experiment results. (a) PI+ICKF. (b) NFTSMC+ICKF. (c) INFTSMC+ICKF.

to simulate the remaining components of the motor system such as IPMSM and inverter, with a real DSP controller of model TMS320F2812. The hardware-in-the-loop semi-physical system used in this paper adopts the structure of actual controller+virtual controlled object to model the controlled object of the system, and the real-time simulator runs the solved model to interact with the real controller. The hardware-in-the-loop semi-physical simulation platform experiments can be used to obtain experimental results consistent with the actual motor. The control algorithm is mainly realized by modifying the algorithm in the Simulink environment and then downloading it to the RT-Lab controller to ensure that the platform parameters and indicators are normal and start running.

Figure 9 shows a slight decrease in the control performance of the experiment compared with Fig. 4. When parameter ingestion occurs in the motor, the overall performance of PI+ICKF and NFTSMC+ICKF is affected, with jitter in speed and large *d-q* current and torque pulsations, but the basic trend and effect comparison is consistent with the simulation results. The A-phase current, *d-q* current, and torque pulsation of PI+ICKF and NFTSMC+ICKF are distorted under ingestion. However, the INFTSMC+ICKF can accurately track the specified speed so that the actual current pulsations and torque pulsations in the *d-q* axis are effectively suppressed, mainly since the IESMDO is better able than the SMO to accurately observe and feed-forward compensation to the controller for unknown disturbance. In summary, INFTSMC+ICKF has the advantages of high anti-disturbance and good robustness under parameter ingestion and unknown perturbation.

6. CONCLUSION

For the problems of overall motor control performance degradation caused by external disturbances and sensor failures in IPMSM drive systems, an ICKF sensor-less INFTSMC algorithm for IPMSM based on ICKF is proposed in this paper. By comparing simulations and experiments under different operating conditions, the algorithm proposed in this article has been verified to have high-precision control performance under unknown disturbances, effectively enhancing the robustness of the system.

ACKNOWLEDGMENT

This work was supported by Postgraduate Scientific Research Innovation Project of Hunan Province under Grant CX20231107.

REFERENCES

1. Zhao, K. H., C. F. Zhang, J. He, X. F. Li, J. H. Feng, et al., "Accurate torque-senseless control approach for interior permanent-magnet synchronous machine based on cascaded sliding mode observer," *The Journal of Engineering*, Vol. 2017, No. 7, 376–384, 2017.
2. Kou, B., X. Zhao, M. Wang, and C. Wen, "Overview of anti-salient permanent magnet synchronous motor and its control technology," *Chinese Journal of Electrical Engineering*, Vol. 39, No. 8, 2414–2425, 2019.
3. Hou, L., H. Shen, Y. Xin, et al., "H_∞ robust control of PMSM speed regulation system," *Transactions of China Electrotechnical Society*, Vol. 34, No. 7, 1478–1487, 2019.
4. Zhao, K., R. Zhou, A. Leng, et al., "Finite control set model-free fault-tolerant predictive control for permanent magnet synchronous motor," *Transactions of China Electrotechnical Society*, Vol. 36, No. 1, 27–38, 2021.
5. Zhao, K., T. Yin, C. Zhang, et al., "Research on model-free sliding mode control of permanent magnet synchronous motor," *Journal of Electronic Measurement and Instrumentation*, Vol. 32, No. 4, 172–180, 2018.
6. Wei, H. and L. Wang, "Adaptive dynamic sliding mode control of permanent magnet linear synchronous motor based on feedback linearization," *Transactions of China Electrotechnical Society*, Vol. 37, No. 4, 861–869, 2022.
7. Sun, B., X. Ge, and Y. Sun, "Dynamical integral sliding mode control for permanent magnet ring torque motor," *Advanced Materials Research*, Vols. 383–390, 799–804, 2011.

8. Tran, M.-D. and H.-J. Kang, "Nonsingular terminal sliding mode control of uncertain second-order nonlinear systems," *Mathematical Problems in Engineering*, Vol. 2015, No. 20, 2015.
9. Chen, S. Y., H. H. Chiang, T. S. Liu, and C. C. Hung, "Precision motion control of permanent magnet linear synchronous motors using adaptive fuzzy fractional-order sliding-mode control," *IEEE/ASME Transactions on Mechatronics*, Vol. 24, No. 2, 741–752, 2019.
10. Xu, B., L. Zhang, and W. Ji, "Improved non-singular fast terminal sliding mode control with disturbance observer for PMSM drives," *IEEE Transactions on Transportation Electrification*, Vol. 7, No. 4, 2753–2762, 2021.
11. Im, J. H. and R. Y. Kim, "Improved saliency-based position sensorless control of interior permanent-magnet synchronous machines with single DC-link current sensor using current prediction method," *IEEE Transactions on Industrial Electronics*, Vol. 65, No. 7, 5335, 2018.
12. Wang, G. R. and J. Y. Li, "Application of modified UKF algorithm in PMLSM sensorless control," *Transducer and Microsystem Technologies*, Vol. 36, No. 2, 158–160, 2017.
13. Zhu, J., X. J. Li, R. B. Fu, et al., "PMLSM without position sensing control of double forgetting Kalman filter," *Journal of System Simulation*, Vol. 30, No. 2, 672–678, 2018.
14. Zhu, J., B. Liu, H. Wang, Z. Li, and Z. Zhe, "Research on sensorless control of PMLSM based on improved volumetric Kalman filter," *Control Engineering*, Vol. 28, No. 3, 471–477, 2021.
15. Song, Y., H. Li, Y. Deng, et al., "Fast super spiral sliding mode control of permanent magnet synchronous motor," *Control Engineering*, Vol. 30, No. 1, 62–69, 2023, doi: 10.14107/j.cnki.kzgc.20200734.
16. Li, X., J. Liu, Y. Yin, and K. Zhao, "Improved super-twisting non-singular fast terminal sliding mode control of interior permanent magnet synchronous motor considering time-varying disturbance of the system," *IEEE Access*, Vol. 11, 17485–17496, 2023, doi: 10.1109/ACCESS.2023.3244190.
17. Zhao, K. H., W. K. Dai, R. R. Zhou, et al., "Novel model-free sliding mode control of permanent magnet synchronous motor based on extended sliding mode disturbance observer," *Proceedings of the CSEE*, Vol. 42, No. 6, 2375–2386, 2022.
18. Zhao, K., W. Liu, Z. Liu, J. Lin, and H. Gang, "A model-free high-order sliding mode control algorithm for permanent magnet synchronous motor," *Journal of Electrotechnical Technology*, 1–14, 2013, doi: 10.19595/j.cnki.1000-6753.tces.220615.
19. Xu, B., L. Zhang, and W. Ji, "Improved non-singular fast terminal sliding mode control with disturbance observer for PMSM drives," *IEEE Transactions on Transportation Electrification*, Vol. 7, No. 4, 2753–2762, 2021, doi: 10.1109/TTE.2021.3083925.
20. Yong, F., B. Sheng, and X. Yu, "Design method of non-singular terminal sliding mode control systems," *Control and Decision*, Vol. 17, No. 2, 194–198, 2002.
21. Xin, G., S. Huang, P. Yu, J. Yang, and H. Wang, "Sliding mode control of IPMSM speed control system based on improved double power reaching law and global fast terminal sliding mode observer," *Journal of Electrical Technology*, Vol. 38, No. 1, 190–203, 2023.
22. Zhang, R., C. Zheng, P. Shi, et al., "Sensorless PMSM control based on improved PSO and generalized fifth-order CKF algorithm," *Journal of Motor and Control*, Vol. 25, No. 7, 120–128, 2021.
23. Guan, B., X. Tang, and Q. Ge, "Square root higher-order volume Kalman filter for unknown measurement noise variance," *Computer Application Research*, Vol. 32, No. 9, 2626–2629, 2015.